Journal of Crystal Growth 365 (2013) 54–58

Contents lists available at SciVerse ScienceDirect

Journal of Crystal Growth

journal homepage: www.elsevier.com/locate/jcrysgro

Crystallization of 640 kg mc-silicon ingots under traveling magnetic field by using a heater-magnet module

Ch. Kudla [b,*], A.T. Blumenau [b], F. Büllesfeld [c], N. Dropka [a], Ch. Frank-Rotsch [a], F. Kiessling [a], O. Klein [d], P. Lange [a], W. Miller [a], U. Rehse [a], U. Sahr [b], M. Schellhorn [b], G. Weidemann [e], M. Ziem [a], G. Bethin [f], R. Fornari [a], M. Müller [b], J. Sprekels [d], V. Trautmann [e], P. Rudolph [g]

[a] Leibniz Institute for Crystal Growth (IKZ), Max-Born-Str. 2, D-12489 Berlin, Germany
[b] SCHOTT Solar Wafer GmbH, Otto-Schott-Str. 13, D-07745, Germany
[c] SCHOTT AG, Hattenbergstr. 10, D-55122 Mainz, Germany
[d] Weierstrass Institute for Applied Analysis and Stochastics (WIAS), Mohrenstr. 39, D-10117 Berlin, Germany
[e] STEREMAT Elektrowärme GmbH, Bouchestr. 12, D-12435 Berlin, Germany
[f] AUTEAM Industrie-Elektronik GmbH, Fredersdorfer Chaussee 38B, D-15370 Fredersdorf-Vogelsdorf, Germany
[g] Crystal Technology Consulting, Helga-Hahnemann-Str. 57, D-12529 Schönefeld (former IKZ Berlin), Germany

ARTICLE INFO

Article history:
Received 9 August 2012
Received in revised form
23 November 2012
Accepted 24 November 2012
Communicated by K.W. Benz
Available online 30 November 2012

Keywords:
A1. Directional solidification
A1. Magnetic fields
A2. Vertical gradient freeze
B2. Multi-crystalline silicon

ABSTRACT

For the first time a heater-magnet module (HMM), simultaneously generating heat and a traveling magnetic field (TMF), was constructed for an industrial scale G5 multi-crystalline Si crystallizer and extensively tested. Effective melt mixing and precise control of the interface shape have been demonstrated using TMF, which resulted in ingots exhibiting superior properties, clearly proving the beneficial effects of the advanced convection control without affecting the stability of the Si_3N_4 crucible coating. Hence, most of the solidified Si volume showed very homogeneous IR transmission without inclusions. Dislocation densities were relatively low and bunching was only rarely observed, resulting in overall high carrier lifetimes. Therefore, our results demonstrate that a HMM configuration in an industrial Si crystallizer may successfully accomplish the following tasks: (i) good thermal stability and controllability of the melt-solid interface morphology, (ii) suppression of second phase inclusions, such as SiC and Si_3N_4, by mastering the mixing of the melt during the whole crystallization process, and (iii) no pronounced interaction between melt and container wall.

1. Introduction

Silicon with its present market share of more than 85% will remain the basic photovoltaic (PV) material also for the next decade. However, due to the very competitive market only high quality silicon wafers are marketable. Today two main technologies have been established to produce PV silicon wafers: the Czochralski technology, which gives high quality mono-crystalline material, and the directional solidification which produces rectangular ingots with comparatively low oxygen content at relatively low cost. Recently, SCHOTT Solar announced the production of mono-crystalline wafers using the latter technique [1] further enhancing its marketability. Indeed, the general challenge for all directional solidification techniques remains the same, namely to obtain ingots with very large grains or, in the limit, quasi-monocrystalline. Due to the multitude of nucleation sites, current efforts are still focused on measures for structural improvement. At the same time, however, the production costs have to be reduced by continuous increase of the ingot dimension. The G4 standard of up to 450 kg silicon load is already scaled up to G5 with 700 kg mass [2] and the roadmap points to a new generation of furnaces with masses of at least 800 kg (G6 and beyond) [3]. As a consequence, several problems become more pressing due to the larger volumes and the higher quality requirements. Major challenges are in particular (i) better control of the melt-solid interface morphology and therewith of the grain structure and dislocation density, (ii) improvement of melt stirring with the aim to control the impurity distribution and prevent foreign particle inclusions, (iii) advanced control of the interaction at the triple point between melt, crystal and container wall to control the nucleation here.

Several vertical Bridgman techniques with numerous model materials are under investigation to control the melt mixing intensity, interface shape and ingot purity, e.g. by applying vibrations [4], external magnetic forces [5], growth or rotation rate variations [6,7]. Among these technological developments,

* Corresponding author. Tel.: +49 3641 681 7010.
E-mail address: christian.kudla@schottsolar.com (Ch. Kudla).

0022-0248/$ - see front matter © 2012 Elsevier B.V. All rights reserved.
http://dx.doi.org/10.1016/j.jcrysgro.2012.11.049

the traveling magnetic field (TMF) has been shown to have very beneficial effects [8,9]. However, the TMF has been employed only on laboratory scale furnaces of cylindrical geometry. No critical issues, such as convection regime, phase boundary bending or external force penetration depths could be reliably analyzed for large industrial systems.

Recently, numerical studies taking into account the Lorentz forces of TMF were performed for the crystallization of rectangular Si ingots [10–12]. A precise coupling of the interface shape to the flow regime was predicted. For large scale industrial application of TMF the KRIST*MAG*® concept proves to be economically favorable [13]. Here heat and TMF are generated simultaneously within the spiral heater surrounding the crucible. Within the framework of the subsequent AVANT*SOLAR* project we reported first experimental results of successful Si crystallization in a rectangular G1 container using such heater-magnet module (HMM) [14]. In this paper we shall report for the first time on the experimental results obtained by applying the KRIST*MAG*® concept to a G5 furnace equipped with a HMM and loaded with 640 kg silicon charge.

2. Experimental

A modular HMM composed of graphite elements, designed [15] to form a rectangular coil around a G5-crucible, was installed in an industrial crystallizer. The coil itself is subdivided into segments with corresponding electrical contacts for the phase-shifted power supply. Based on electromagnetic calculations a suitable power supply including control and visualization has been developed for the HMM as already mentioned in Ref. [13]. Both a three-phase alternating current (AC) of desired frequency (f=10–600 Hz) and phase shift (φ=0–360°) for TMF generation and a direct current (DC) component for controlling the melting and crystallization process are simultaneously supplied to the heater-magnet. In consequence, Lorentz force densities F_L up to 10^3 N/m^3 are present in the melt in case of the maximum current I of 500 A per coil section. Normally, weaker Lorentz forces of some 10 N/m^3 are actually used during crystallization.

As starting material 640 kg uncompensated electronic grade silicon was used with a varying B-dopant atomic fraction between 2×10^{-7} and 3×10^{-7} for the different ingots. The silicon was heated in a Si_3N_4 coated quartz crucible beyond its melting temperature and held at the temperature for several hours. During this period the DC was modulated by AC-driven down- or upward directed TMF to induce an intensified melt mixing for homogenization purposes and SiO degassing. Subsequently, the unidirectional solidification was started at typical growth rates at the container bottom by balanced cooling down due to reduced power in the coil segments. In most cases the TMF parameters were varied at the beginning of the crystallization and either kept constant or varied continuously during the whole process. TMF of different direction, frequency and current were used to induce favorable melt mixing patterns and different interface shapes. Additionally, tests under double-frequency TMF mode, the fundamentals of which were described elsewhere [16,17], have been performed to maximize the flow speed towards the container center and minimize the friction at the wall. Finally, for sake of comparison, few experiments under DC only, i.e. without any non-steady magnetic field components, were also carried out.

The as-grown ingots were cut into 25 standard sized 6 in. bricks, each of which was investigated by IR transmission, minority carrier lifetime of several selected area samples as well as resistivity and minority carrier lifetime line scans. The interface shape of all ingots was determined via striation analysis by lateral photovoltage scanning (LPS) [18] of half cross sections of the ingot ranging from the center to the outer rim. In selected cases even complete cross sections were cut out, revealing very symmetrical growth over the whole width of the ingot and during the whole process. This confirms that very symmetrical thermal and magnetic fields were established during growth. Grain boundaries and dislocation structures (counting of etch pit density, EPD), were determined by KOH and Sirtl etching, respectively. Finally, concentrations of interstitial oxygen and substitutional carbon were detected by Fourier transform infrared spectrometry (FTIR).

3. Numerical simulation

Generally, all experiments were accompanied by 3D simulations of flow-dynamics (CFD) and magnetic forces using the commercial code ANSYS CFX 13.0 and ANSYS Emag. The results of global thermal analyses provided thermal boundary conditions (BCs) for the local simulation of the melt flow. Radiative heat transfer in the furnace was described by discrete transfer radiation method. Effects of turbulence were taken into account by using the kω SST model. Buoyancy driven flow was used as an initiation and as a benchmark. Both temperature fields and melt flow structures for various TMF driven flows were determined. After growth, the interface shape as determined by LPS was compared with the simulated one. A good agreement between simulation and experimental results was observed.

Fig. 1 shows a characteristic convection pattern within the melt exposed to a TMF in downward direction. The flow acceleration and

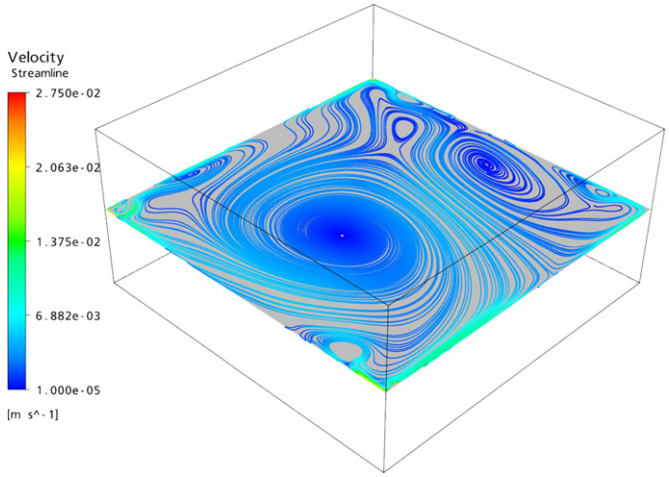

Fig. 1. Streamlines of the convection pattern within the silicon melt inside of a G5 crucible exposed to a TMF of downward direction.

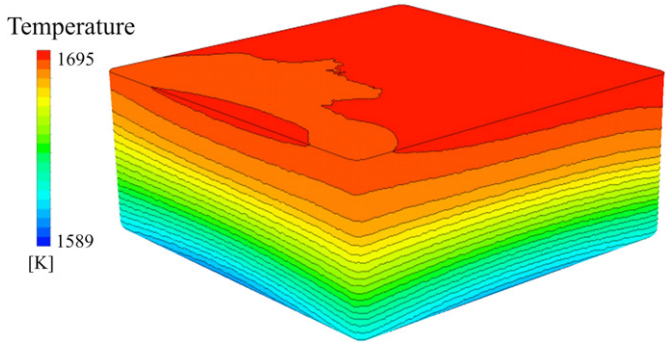

Fig. 2. Temperature field within the silicon melt inside of a G5 crucible exposed to downward TMF indicating the slightly convex bending of the interface due to Lorentz force induced convection.

stirring enhancement were obtained in a TMF regime relative both to: (i) pure buoyancy and to (ii) magnetic driven flows in steady (DC supply) and alternating unsteady magnetic fields (AC supply with $\Delta\varphi=0^{\circ}$). A snapshot of the 3D thermal field in a downward TMF of selected frequency and phase shift is given in Fig. 2 indicating the form of the melt-solid interface. Bending of the interface towards convexity appeared due to the Lorentz force induced convection curl at the crucible rim. In a previous paper we have already demonstrated the advantages of the double-frequency TMF consisting of superimposed upward and downward TMF of different frequencies [17]. Due to the different skin effect, the high frequency component acts mainly at the melt periphery whereas the low-frequency one results in a Lorentz force extended into the central melt region. Thus, the shift of the maximum of the Lorentz force density and consequently the shift of the flow rate maximum away from the crucible walls towards melt center stabilized the crucible coating markedly.

Our calculations proved to be very helpful to determine the process parameters for ensuring optimal mixing and the desired interface morphology during the whole crystallization process.

4. Experimental results and discussion

A 640 kg silicon ingot crystallized under TMF is shown in Fig. 3. The ingot shows no signs of adhesion to the container wall and displays a smooth upper surface. The TMF induced convection close to the container wall obviously has no negative effect on the Si_3N_4 coating of the crucible. Furthermore, the melt velocity close to the container wall can even be reduced when a double-frequency TMF is used.

Furthermore, measured residual carbon and oxygen concentrations along the solidification direction show typical values. For instance, such ingot shows decreasing oxygen content from the bottom to the top between 7.5 and 1.2×10^{17} atoms/cm^3 and relatively uniform carbon contents of $3.5–3.9\times10^{17}$ atoms/cm^3.

Fig. 4 shows LPS images of partial cross sections taken from two ingots grown within the same thermal field but with different magnetic induction forces. One ingot was grown using only DC and the other with TMF provided by a phase shifted AC. Weak striations are visible in both cases permitting to determine the interface curvature. However, the striations are less defined and generally more homogeneous in case of the ingot grown within a TMF indicating a very stable growth process. As can be seen on top of Fig. 4, a nearly flat interface with unfavorable concave rim region is given by the thermal field when only the negligible external Lorentz forces of the DC are applied. In contrast, a convex crystallization front with a favorable flattening at the container wall is obtained (Fig. 4, bottom) due to the presence of Lorentz force driven vortices in the rim region of the melt exposed to downward directed TMF (see also Fig. 2). Furthermore, the stability of the TMF driven crystallization is confirmed by the resistivity measurements shown on the right side of Fig. 5. The resistivity being inversely proportional to the boron concentration in the solidified silicon shows a monotonic decline over the whole height of the brick. Obviously boron was incorporated under conditions of complete melt mixing, thus showing good agreement with Scheil's law [19]. In comparison, ingots solidified without a TMF show markedly different resistivity curves as given for example on the left side of Fig. 5. Here, the resistivity curves do not run uniformly and presents a series of flat and steep segments. As it is well known, this is a sign of volatile boron incorporation occurring when—at least occasionally—insufficient melt convection takes place resulting in a rising boron concentration at the crystallization front.

Fig. 6 compares IR transmission images of bricks from the center of two ingots grown with and without TMF. Only a few centimetres after the onset of crystallization under DC the structure is markedly degraded due to the beginning of morphological interface instability (Fig. 6, left). This harmful effect is caused by constitutional supercooling and does appear when

Fig. 3. 640 kg silicon ingot crystallized under TMF showing no signs of adhesion to the container wall and smooth upper surface.

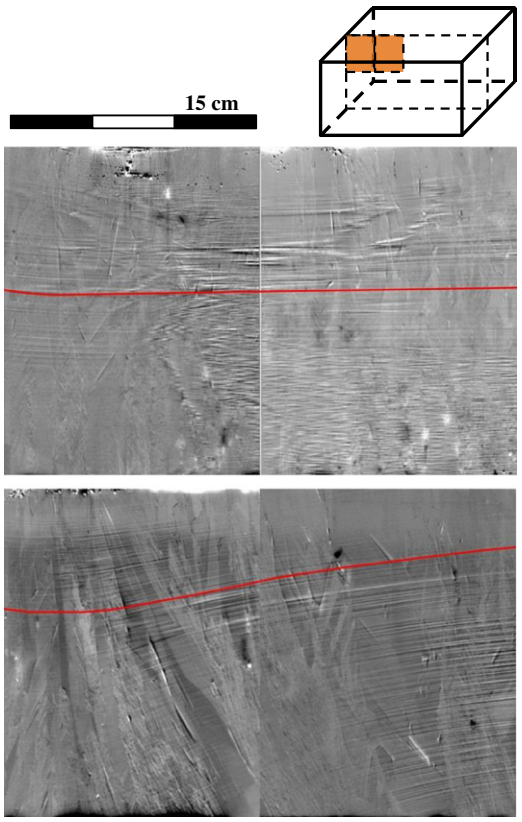

Fig. 4. LPS images of partial cross sections (see inserted sketch) taken from two ingots grown within the same thermal field but different magnetic fields. The upper image was taken from an ingot grown without TMF, the lower from an ingot exposed to downward TMF. Light striations are visible in both cases permitting to determine the interface curvature.

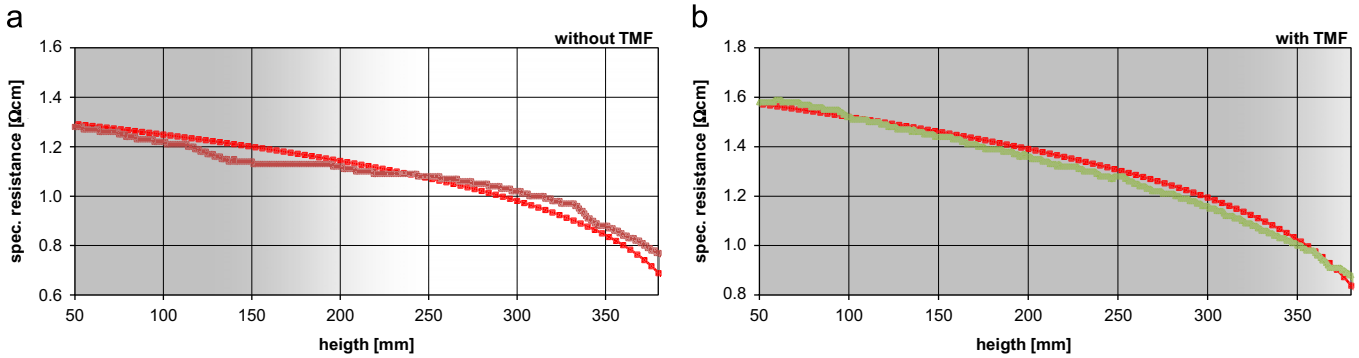

Fig. 5. Resistivity measurements of two bricks cut out of different ingots grown without (left) and with (right) TMF. Only in case of the ingot grown within a TMF the measurements show good agreement with Scheil's law (red line) (For interpretation of the references to color in this figure legend, the reader is referred to the web version of this article.).

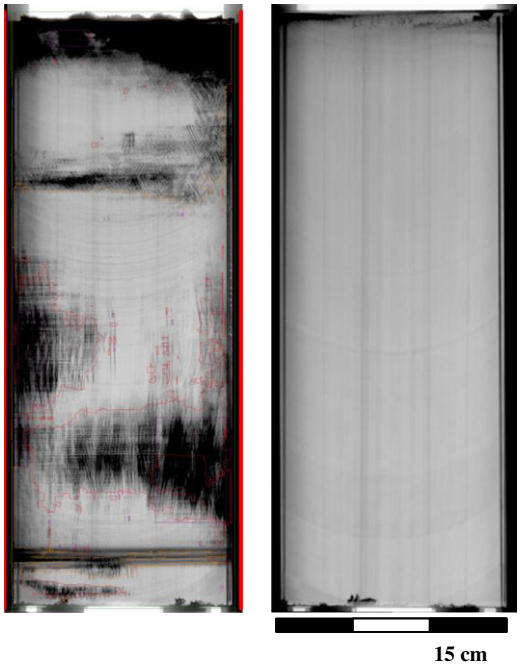

Fig. 6. IR transmission images of bricks from the center of two ingots grown without and with TMF. The structure is markedly degraded in case of DC only (left) while the ingot grown in a TMF shows homogeneous structural and chemical quality along the whole bricks height (right).

impurity accumulation takes place in front of the solid/liquid interface as a result of scarce melt convection [20]. This leads to a large diffusion boundary layer enriched by residual impurities, such as N and C. As soon as the concentration of these impurities exceed their respective solubility limits, SiC and Si_3N_4 precipitates form in proximity of the solidification front and are incorporated into the solid phase. Both structural defects and presence of secondary phase particles degrade the ingot quality considerably and inhibit IR transmission. Opposite to that, ingots grown in a TMF show homogeneous structural and chemical properties along the whole bricks height as can be seen in Fig. 6, right. Only a small area at the very top of the ingot lacks transparency in IR transmission due to higher levels of foreign impurity and particle inclusion. In VGF ingot crystallization this is a common effect, which mainly stems from impurity segregation with a steep increase in concentration at the very top of the ingot—when the last small fraction of the melt freezes. Obviously the TMF generated convection swirl predicted by our numerical simulations (Fig. 1) very effectively helps to reduce the undesirable diffusion boundary layer.

Fig. 7 shows details of grain structure, dislocation distribution and mapped carrier lifetime of three back-to-back slices cut out of a center brick of an ingot grown in a double-frequency TMF. The columnar grain structure parallel to the growth direction in Fig. 7(a) shows several large grains—some of them having a width of more than one cm. Additionally, only relatively few dislocation bundles can be observed in Fig. 7(b). While the mean EPD of the bundle-free regions is about $1 \times 10^4\,cm^{-2}$, enhanced values of 1.8–3.8 $10^5\,cm^{-2}$ have been determined within the bundles but still significantly lower than values reported by Wang [21] and Schmidt [22] of up to $10^6\,cm^{-2}$. Consequently, very high carrier lifetimes over 35 μs are measured in most sections on the polished surface shown in Fig. 7(c). The enhanced minority carrier lifetime can as well be demonstrated by the data given in Fig. 8 measured on the as cut surface of the central brick of ingots grown with and without TMF. The ingot grown without TMF has an average lifetime of 3.8 μs, a maximum well below 6 μs and surpasses 4 μs at 100 mm height. Then again, the ingot grown in a 2f-TMF shows an average lifetime of 5.8 μs with maximum values above 8 μs surpassing 4 μs at a height of approximately 60 mm. For better comparison data is given as well for an ingot grown within a similar setup but a conventional resistance heater. While the average value of 5.0 μs is better than in case of the HMM setup without TMF it is still significantly lower than those values found in case of a 2f-TMF.

5. Conclusions

In summary, we successfully integrated a heater–magnet module for simultaneous generation of heat and traveling magnetic fields into an industrial scale G5 VGF-crystallizer. For comparison, several silicon ingots of 640 kg mass were solidified with and without TMF. The TMF ingots exhibited superior properties, clearly proving the beneficial effects of an advanced convection control. On the other hand, TMF did not affect the mechanical/compositional stability of the Si_3N_4 crucible coating and hence smooth ingot surfaces have been observed.

Effective melt mixing and precise control of the interface shape have been achieved using TMF, which resulted in very homogeneous IR transmission without second phase inclusions in most of the solidified volume. Dislocation densities were relatively low and bunching was only rarely observed, resulting in overall high carrier lifetimes. Therefore, our results demonstrate that a TMF implemented according to the KRIST*MAG*® configuration in an industrial Si crystallizer may successfully accomplish the following tasks: (i) good thermal stability and controllability of the melt-solid interface morphology, (ii) suppression of second phase inclusions, such as SiC and Si_3N_4, by mastering the mixing

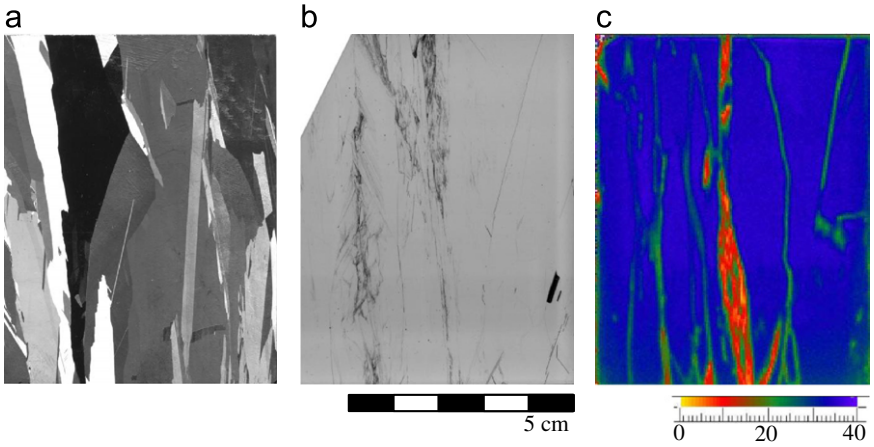

Fig. 7. Comparison of grain structure (a), dislocation density (b) and minority carrier lifetime (c) of a selected area in the central brick of an ingot grown with a TMF.

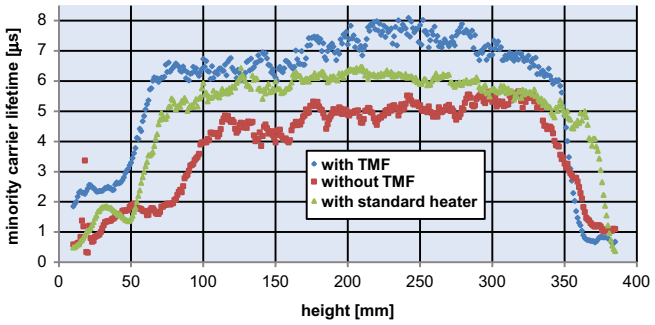

Fig. 8. Comparison of minority carrier lifetime measured on the as-cut brick for ingots grown with and without TMF and an ingot grown with a conventional resistance heater.

of the melt during the whole crystallization process, and (iii) no pronounced interaction between melt and container wall.

Acknowledgments

The authors are indebted to M. Czupalla, A. Lüdge, U. Juda, M. Naumann, M. Pietsch and O. Root from IKZ, W. Dreyer from WIAS, T. Mono from Schott Solar, A. Koza from Steremat, B. Eberhardt from Auteam, M. Kittler and W. Seifert from IHP Frankfurt, and B. Nacke from Leibniz University Hanover for their essential contributions to the project results.

The AVANT*SOLAR* was supported by the State of Berlin in the framework of the "Zukunftsfonds Berlin" and the Technology Foundation Innovation Center Berlin (TSB) as well as the "Zukunftsagentur" of the State Brandenburg. It was co-financed by the European Union within the European Regional Development Fund (EFRE) and Schott Solar Wafer GmbH.

References

[1] 〈http://www.schottsolar.com/de/news/aktuelle-nachrichten/article/quasimono-mit-199-p/〉.
[2] M. Müller et al., Challenges of mc-Si solar wafer manufacturing, German Polish Conference on Crystal Growth 2011 (GPCCG 2011), Frankfurt-Oder, 15-19-03.
[3] Y. Wan, T. Zhang, D. You, J. Du, G. Xiao, D. Zhong, Proceedings of the Sixteenth International Conference on Crystal Growth (ICCG-16), 08–13 August 2010 in Beijing, PR China, 〈http://210.72.154.189/Prelim_Abstract_Display.php?EID=1734〉.
[4] E.V. Zharikov, in: P. Capper, P. Rudolph (Eds.), Crystal Growth Technology: Semiconductors and Dielectrics, Wiley-VCH, Weinheim, 2010, pp. 41–64.
[5] P. Rudolph, K. Kakimoto, MRS Bulletin 34 (4) (2009) 251–258.
[6] M. Trempa, C. Reimann, J. Friedrich, G. Müller, Journal of Crystal Growth 312 (2010) 1517–1524.
[7] M.P. Bellmann, E.A. Meese, L. Arnberg, Journal of Crystal Growth 318 (2011) 239–243.
[8] I. Grants, G. Gerbeth, Journal of Crystal Growth 310 (2008) 3699–3705.
[9] Ch. Frank-Rotsch, P. Rudolph, Journal of Crystal Growth 311 (2009) 2294–2299.
[10] M. Zschorsch, K. Dadzis, U. Wunderwald, Th. Jung, J. Friedrich, Proceedings of the Third International Workshop on Crystalline Silicon Solar Cells (CSSC-3), SINTEF/NTNU, 03–05 June 2009 in Trondheim, Norway, pp. 1–4.
[11] C. Tanasie, D. Vizman, J. Friedrich, Journal of Crystal Growth 318 (2011) 293–297.
[12] N. Dropka, W. Miller, R. Menzel, U. Rehse, Journal of Crystal Growth 312 (2010) 1407–1410.
[13] P. Rudolph, J, Journal of Crystal Growth 310 (2008) 1298–1306.
[14] F.-M. Kiessling, F. Büllesfeld, N. Dropka, Ch. Frank-Rotsch, M. Müller, P. Rudolph, Journal of Crystal Growth (2012).
[15] P. Lange, M. Ziem, P. Rudolph, Patent Description DE, 10 (2009) 045 680.
[16] F. Büllesfeld, U. Sahr, W. Miller, P. Rudolph, U. Rehse, N. Dropka, Patent DE 10 (2008) 059 521 B4, WO/2010/060802B1.
[17] N. Dropka, W. Miller, U. Rehse, P. Rudolph, F. Büllesfeld, U. Sahr, O. Klein, D. Reinhardt, Journal of Crystal Growth 318 (2011) 275–279.
[18] N.V. Abrosimov, A. Lüdge, H. Riemann, W. Schröder, Journal of Crystal Growth 237–239 (2002) 356–360.
[19] E. Scheil, Zeitschrift fur Metallkunde 34 (1942) 70–73.
[20] W.A. Tiller, K.A. Jackson, J.W. Rutter, B. Chalmers, Acta Metallurgia 1 (1953) 428–437.
[21] T.Y. Wang, S.L. Hsu, C.C. Fei, K.M. Yei, W.C. Hsu, C.W. Lan, Journal of Crystal Growth 311 (2009) 263–267.
[22] E. Schmid, S. Würzner, C. Funke, V. Galindo, O. Pätzold, M. Stelter, Journal of Crystal Growth 359 (2012) 77–82.